Li et al. Nanoscale Research Letters (2016) 11:470
DOI 10.1186/s11671-016-1685-1

Nanoscale Research Letters

NANO EXPRESS Open Access

# The Sensing Properties of Single Y-Doped $SnO_2$ Nanobelt Device to Acetone

Xinmin Li[1,3], Yingkai Liu[1,2,3*], Shuanghui Li[1,3], Jieqing Huang[1,3], Yuemei Wu[1,3] and Dapeng Yu[3,4]

**Abstract**

Pure $SnO_2$ and Y-doped $SnO_2$ nanobelts were prepared by thermal evaporation at 1350 °C in the presence of Ar carrier gas (30 sccm). The samples were characterized by scanning electron microscope (SEM), X-ray diffraction (XRD), energy dispersion spectrometer (EDS), X-ray photoelectron spectrometer (XPS), UV-Vis absorption spectroscopy, Raman spectroscopy, and Fourier transform infrared spectrum (FTIR). The sensing properties of the devices based on a single $SnO_2$ nanobelt and Y-doped $SnO_2$ nanobelt were explored to acetone, ethanol, and ethanediol. It reveals that the sensitivity of single Y-doped $SnO_2$ nanobelt device is 11.4 to 100 ppm of acetone at 210 °C, which is the highest response among the three tested VOC gases. $Y^{3+}$ ions improve the sensitivity of $SnO_2$ sensor and have an influence on the optical properties of Y-doped $SnO_2$ nanobelts.

**Keywords:** $SnO_2$ nanobelts, $Y^{3+}$ doping, Gas sensor, Optical properties, Acetone

## Background

With the development of science and technology as well as people's increasing concerns for the environment, considerable attentions are paid to efficiently and precisely detect and supervise flammable, explosive, or poisonous gases [1].

As a transparent n-type semiconductor with a band gap of 3.6 eV, $SnO_2$ can be used as photoelectric devices, sensors, catalysts, and other functional materials [2]. Due to the unique physicochemical properties of $SnO_2$ and enhanced sensing properties of nanostructured materials, quasi-one-dimensional (1D) $SnO_2$ nanomaterials are being widely studied [3]. Various methods were developed to synthesize nanostructured $SnO_2$ materials, such as the sol-gel method, liquid precursor method [4], electroplating tin thermal oxidation method [5], and chemical vapor deposition (CVD) method [6]. Therefore, synthesis of 1D nanostructured $SnO_2$ materials has made great achievements [7, 8]. $SnO_2$ with various morphologies such as nanoparticle, nanowire, nanosilk, nanosawtooth, nanobelt, or nanotube are obtained by the abovementioned methods [9–11], which can be used as building blocks for functional devices [12, 13]. Inherent small size effect and surface effect of nanomaterials make $SnO_2$ possess particular physicochemical properties, which are beneficial for gas sensors and solar cells [14–17].

From the point view of pollution, acetone (a common reagent used widely in industries and labs) is harmful to human health. It is extensively used to dissolve plastic, purify paraffin, and dehydrate tissues in pharmaceutics [18]. Inhalation of acetone causes headache, fatigue, and even narcosis and harmfulness to the nerve system. Hence, it is necessary to monitor acetone concentration in the environment for health and safety purposes in the factory [19].

In this work, we undertake the study on the fabrication and characterization of the devices based on a single $SnO_2$ nanobelt (NB)/Y-$SnO_2$. After that, we systematically investigate the sensing properties of single $SnO_2$ NB/Y-$SnO_2$ NB device. Based on it, the influence of Y elements on the sensing properties of $SnO_2$ NB is discussed.

## Methods

### Synthesis of Y-Doped $SnO_2$ NBs

Y-doped $SnO_2$ NBs (hereafter denoted as "Y-$SnO_2$ NBs") were prepared by thermal evaporation technique. For synthesis of Y-$SnO_2$ NBs, $SnO_2$ powders with a purity of 99.99 % were mixed with Y powders (Yttrium (III)

* Correspondence: ykliu@ynnu.edu.cn
[1]Key Laboratory of Yunnan Higher Education Institutes for Optoelectronic Information and Technology, Kunming 650500, People's Republic of China
[2]Key Laboratory of Yunnan Normal University for Photoelectric Materials & Device, Kunming 650500, People's Republic of China
Full list of author information is available at the end of the article

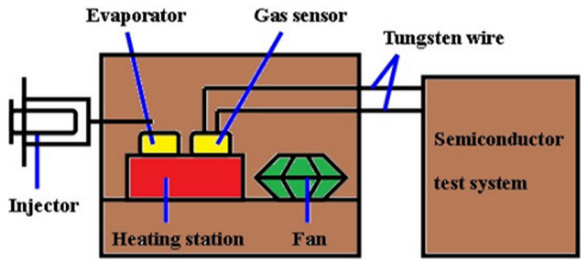


**Fig. 1** The schematic diagram of the test system

acetate tetrahydrate 99.99 %) in the weight ratio of 20:1 and then put into a ceramic boat. The boat was placed in the center of the alundum tube, which was installed in a high-temperature furnace. A silicon substrate coated with about 10-nm-thick Au film was put in the alundum tube with a distance of 10 cm from the ceramic boat and then the tube was cleaned several times by argon gas. The temperature of the furnace was heated up to 1350 °C at a rate of 15 °C/min and was kept for 2 h. Ar gas was flowed at 30 sccm, and the pressure inside the tube was maintained to 112.5 Torr during the whole experiment. The deposited samples were taken out as the furnace was naturally cooled to room temperature.

The morphology, microstructures, and composition of Y-$SnO_2$ NBs were characterized by X-ray diffraction (XRD), scanning electron microscopy (SEM), energy dispersive X-ray spectroscopy (EDS), transmission electron microscopy (TEM), UV-Vis absorption spectra, Raman spectra, Fourier transform infrared spectrum (FTIR), and high-resolution transmission electron microscopy (HRTEM).

The device was fabricated as follows: for fabrication of a single nanobelt sensor, $SnO_2$ NBs and Y-$SnO_2$ NBs were scratched by tweezers and some products were dispersed in ethanol, respectively. The resulting suspension was dropped onto the silicon substrate with a 500-nm-thick $SnO_2$ layer. After the ethanol evaporated completely, Ti (8 nm) and Au (100 nm) electrodes were deposited by dual-ion beam deposition system (LDJ-2a-F100-100 series) with the assistance of a meshgrid mask composed of tungsten wires (10 μm in diameter). The vacuum was kept at $2.2 \times 10^{-2}$ Pa in the whole process, and Ar was flowed at 10 mA/cm$^2$. The sensing test system is illustrated in Fig. 1. The measurements were conducted in a hermetic stainless steel vessel (20 L). Then, the sensor linked with the semiconductor test system by tungsten wires was put on a heating station. The target liquid would be injected into an evaporator to quickly evaporate, and a fan was used to produce homogeneous atmosphere in the chamber. Finally, the gas sensing performance of the devices was measured by Keithley 4200.

## Results and Discussion

### Morphology and Structure

The morphology of the Y-$SnO_2$ was observed by scanning electron microscopy, as shown in Fig. 2a. The products are nanobelts, which are randomly stacked together; many filamentous structures were presented. A high-magnification SEM image in Fig. 2b reveals that the obtained NBs are of smooth surfaces with a thickness of 30–50 nm and length up to 40 μm. HRTEM image of a Y-$SnO_2$ NB is displayed in Fig. 2c and the

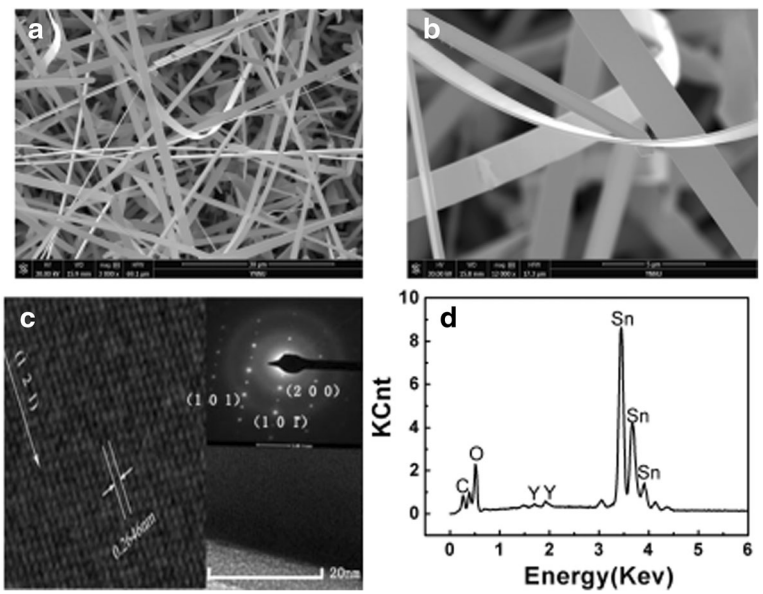


**Fig. 2** Low-magnification SEM image (**a**). High-magnification SEM micrograph of Y-$SnO_2$ nanobelts (**b**). HRTEM image, the *inset*: SAED pattern (**c**). EDS pattern of Y-$SnO_2$ NBs (**d**)

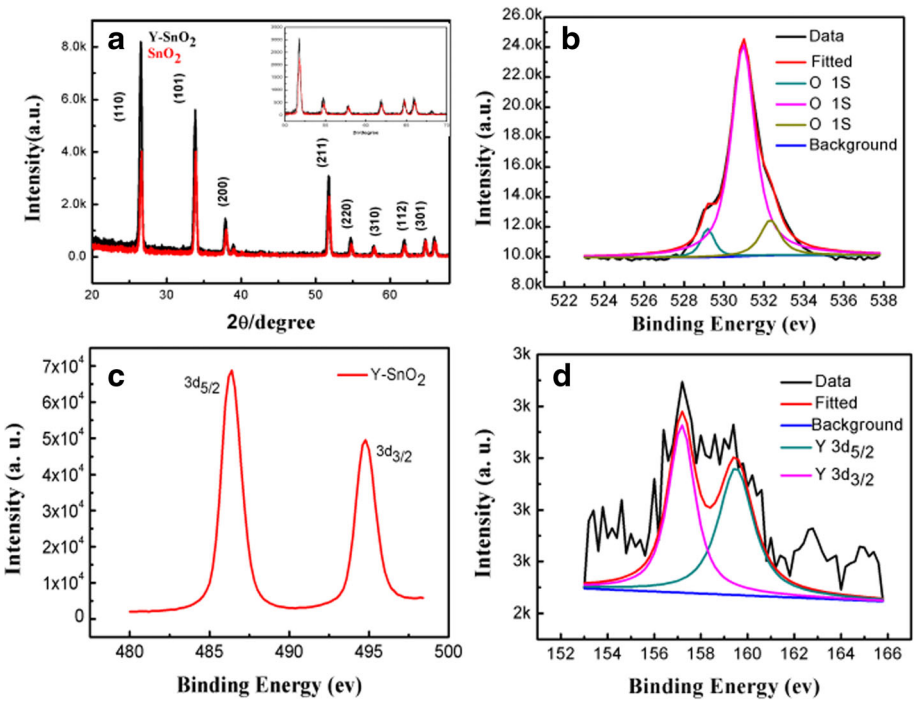


**Fig. 3** XRD patterns of Y-$SnO_2$ and undoped $SnO_2$ (**a**). XPS spectrum of superposed O (1s) (**b**), Sn (3d) (**c**), and Y (3d) (**d**), respectively

interplanar spacing is 0.2646 nm, and the growth direction is along [−121]. The EDS pattern of a Y-$SnO_2$ nanobelt was shown in Fig. 2d. The elements of C, O, Sn, and Y were observed in EDS. It confirms the existence of $Y^{3+}$ in the nanobelt and the content of Y is 0.86 wt.%.

The XRD and XPS pattern of Y-$SnO_2$ NBs and undoped counterparts are presented in Fig. 3. It is found that all well-defined diffraction peaks can be indexed as the tetragonal structure $SnO_2$ with lattice parameters $a = b = 0.4738$ nm, $c = 0.3188$ nm (JCPDS card no. 71-0467). The positions of the diffraction peaks ($2\theta =$ 26.5°, 33.7°, 37.8°, 51.8°, 54.8°, 57.7°, 61.8°, and 64.6°) matched with the crystal plane ((110), (101), (200), (211), (220), (310), (112), and (301), respectively). No other impurities are detected, indicating that the doping of Y element does not cause the change of crystal structures. Comparing with XRD of pure $SnO_2$, the diffraction peaks of Y-$SnO_2$ NBs corresponding to (211), (220), (310), (112), and (301) lattice planes shift towards the low-angle direction, as shown in the inset of Fig. 3a. The reason is that $Y^{3+}$ ions (radius 89 pm) replace the position of $Sn^{4+}$ (radius 69 pm); the lattice parameters of Y-$SnO_2$ NBs become larger than those of pure $SnO_2$, revealing that $Y^{3+}$ ions have been doped into the lattices of $SnO_2$.

The XPS spectra for the binding energy of Sn (3d), O (1s), and Y (3d) electrons are also provided to demonstrate the existence of $Y^{3+}$ ions. The deconvolution of the O (1s) peak shows three Gaussian peaks, centered at 529.3, 530.98, and 532.5 eV, respectively (displayed in Fig. 3b). The peak at the low-binding energy can be attributed to the lattice oxygen in $SnO_2$ and the high-binding energy related to the chemisorbed oxygen species. The Sn (3d) peak shows two peaks located at the binding energies of 486.3 eV Sn ($3d_{5/2}$) and 494.7 eV of Sn ($3d_{3/2}$), as shown in Fig. 3c. The separation distance between the two peaks is 8.4 eV, which corresponds to the Sn standard spectrum, indicating the formation of $Sn^{4+}$ oxidation state in the $SnO_2$ nanobelts [20]. The Y (3d) can be separated

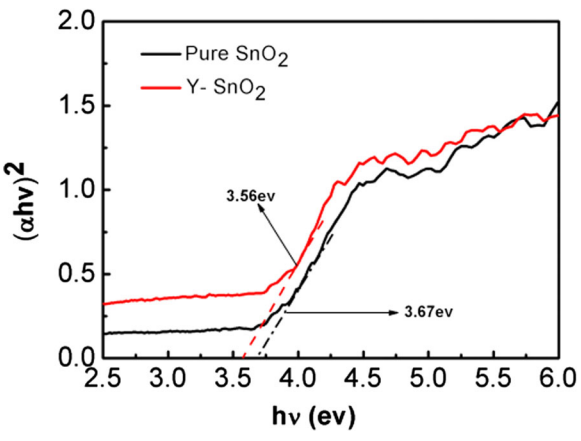


**Fig. 4** UV-Vis absorption spectra of Y-$SnO_2$ nanobelts and pure $SnO_2$ nanobelts. The corresponding $(\alpha h\nu)^2$ versus hν curves

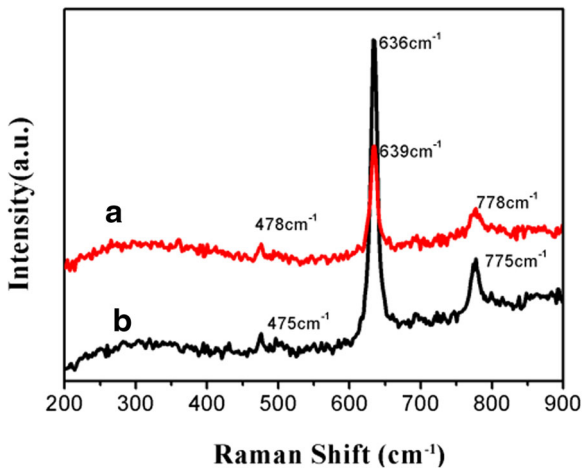


**Fig. 5** Raman spectra of Y-$SnO_2$ NBs (*a*) and pure $SnO_2$ NBs (*b*)

into two peaks; the peaks at 157.2 and 159.98 eV belong to the binding energies of Y ($3d_{5/2}$) and Y ($3d_{3/2}$), respectively, as displayed in Fig. 3d. These results are in good agreement with those of XRD and EDS. Therefore, it is confirmed that $Y^{3+}$ ions are doped into $SnO_2$ nanobelts successfully.

## Optical Properties

The UV-Vis absorption spectra of Y-$SnO_2$ NBs and pure $SnO_2$ NBs are presented in Fig. 4. The energy band gap was determined to be 3.56 eV for the Y-$SnO_2$ NBs and 3.67 eV for the pure $SnO_2$ ones, respectively. Compared with that of pure $SnO_2$, the UV-Vis absorption peak of Y-$SnO_2$ NBs redshifts after doping. Impurity energy levels in the band gap will change into impurity bands due to the interaction between the impurity ions and the based lattices [21, 22].

Figure 5 shows the Raman spectra of pure and Y-$SnO_2$ NBs measured at room temperature. It is seen that three peaks of Y-$SnO_2$ NBs can be observed in Fig. 5a, which are located at 478, 639, and 778 $cm^{-1}$, respectively. In the meantime, we also found that the intensity of the Raman peak centered at 300 $cm^{-1}$ for Y-$SnO_2$ NBs is slightly higher than that of its counterpart. Compared with pure $SnO_2$ in Fig. 5b, its spectrum has not changed much after doping. However, it is noted that the Raman peaks of Y-$SnO_2$ NBs happen to redshift by the quantitative analysis. The intensity difference of Raman peaks for the pure $SnO_2$ NBs and Y-$SnO_2$ NBs can be attributed to the crystalline sizes of the samples [23].

## Sensing Properties

Figure 6a shows a typical optical microscope image of the obtained Y-$SnO_2$ NB and pure $SnO_2$ NB device, which is composed of an individual nanobelt and Au electrodes. Figure 6b, c presents the SEM image of Fig. 6a, which is used for all gas sensing measurements. The thickness of Y-$SnO_2$ NB and pure $SnO_2$ NB is about 50 nm. The length and width of the pure $SnO_2$ NB and

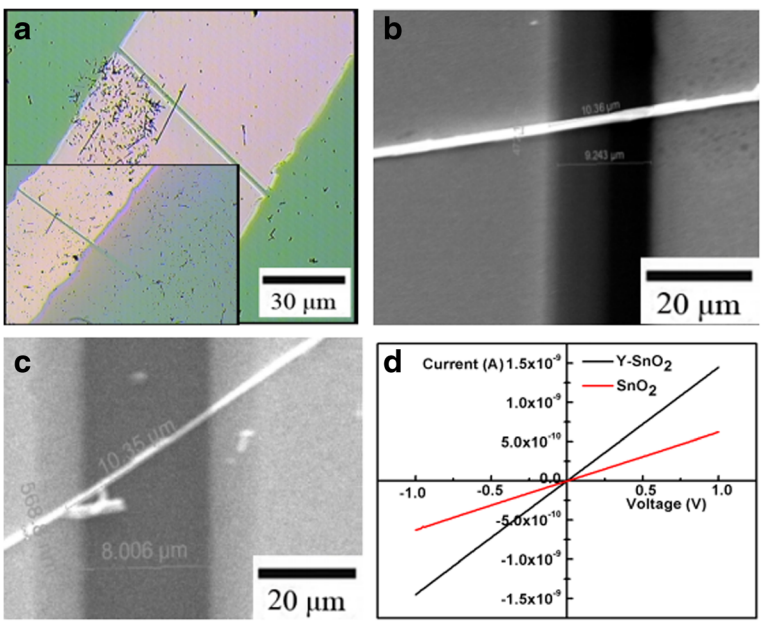


**Fig. 6** The optical microscopic image of the pure $SnO_2$ NB. *Inset*: the optical microscopic image of the Y-$SnO_2$ NB (**a**); SEM image of a single $SnO_2$ NB (**b**); SEM image of a single Y-$SnO_2$ NB (**c**); I–V curves of the pure $SnO_2$ and Y-$SnO_2$ NB devices (**d**)

Y-$SnO_2$ NB are about 10.36 and 10.35 μm and 472.1 and 568.8 nm, respectively. The calculated results confirmed that the surface ratio of Y-$SnO_2$ NB to pure $SnO_2$ NB is 1.1 (see Additional file 1 for more details). Figure 6d shows the I–V curves of pure $SnO_2$ and Y-$SnO_2$ nanobelt in air at room temperature. It shows that the curves are nearly linear, revealing good Ohmic contacts between $SnO_2$ NB and Y-$SnO_2$ NB with the electrodes. The resistance of $SnO_2$ NB is about $2.01 \times 10^9\ \Omega$ and that of Y-$SnO_2$ NB is about $6.69 \times 10^8\ \Omega$. The ratio of their resistance is about 3, which is much larger than that of their surface ratio. Therefore, the dopant improves the conductance of Y-$SnO_2$ NB.

Figure 7a shows the sensitivity of the Y-$SnO_2$ NB device as it is exposed to 100 ppm of ethanediol, ethanol, and acetone gases at different operating temperatures from 50 to 300 °C. It is noted that the sensitivity increases with an increment of the temperature up to 210 °C, and then starts to fall. Therefore, the optimum working temperature of sensor to ethanediol, ethanol, and acetone gases is 210 °C with a response of 11.4 to acetone. The histogram of the Y-$SnO_2$ NB device corresponding to 100 ppm of different gases at 210 °C is shown in Fig. 7b. The response to 100 ppm of acetone is 11.4 at 210 °C, which is 2.7 times and 4.7 times as large as to ethanol and ethanediol, respectively. Under the condition of the same concentration of acetone, its response is 9.04 times as large as that of its pure counterpart. The result reveals that the response of Y-$SnO_2$ NB sensor to acetone gas has good selectivity. Figure 7c

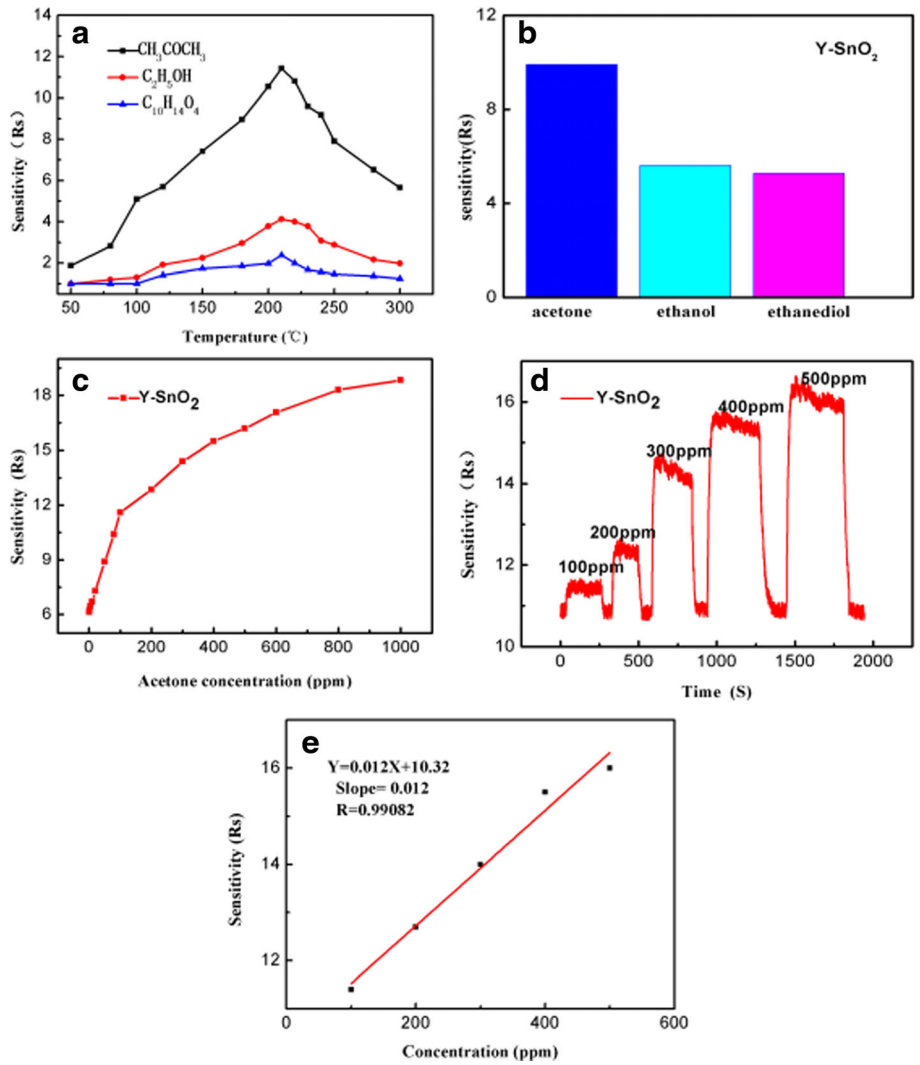


**Fig. 7** The sensitivity curves of the Y-$SnO_2$ NB (**a**). The histogram of the Y-$SnO_2$ NB device corresponding to 100 ppm of different gases at 210 °C (**b**). The response of the Y-$SnO_2$ NB sensor is further investigated as a function of acetone gas concentration at 210 °C (**c**). The response (recovery) time of the Y-$SnO_2$ NB device (**d**). Fitting the curve of response versus acetone concentration in the range of 100–500 ppm (**e**)

shows that the response of Y-$SnO_2$ NB sensor is further investigated as a function of acetone concentration at 210 °C. It is seen that the sensitivity increases with an increase of acetone concentration from 0 to 100 ppm, and then slowly becomes from 100 to 800 ppm, and finally nearly reaches a saturated state from 800 to 1000 ppm. It is also observed that the resistance of $SnO_2$ NB declines significantly upon injection of acetone gas and returns to its original state when acetone vapor is expelled, as shown in Fig. 7d. The response (recovery) time is about 9–25 s/10–30 s to acetone at 210 °C. Repeated measurements have corroborated that the Y-$SnO_2$ NB device possesses good selectivity and stability to acetone. Figure 7e shows the fitting curve of the sensitivity versus acetone concentration in 100–500 ppm. Its slope is 0.012 $ppm^{-1}$ with a correlation coefficient $R$ of 0.9908. One hundred forty data points in Fig. 7d at the baseline were selected to calculate a standard deviation ($S$ = 0.0428). According to $RMS_{noise} = \sqrt{S^2/N}$, the $RMS_{noise}$ is 0.0036 for acetone sensor [24]. The detection limit can be written as DL (ppm) = 3 × $RMS_{noise}$/slope, where 3 is the signal-to-noise ratio and $RMS_{noise}$ represents the sensor noise [20]. Therefore, the detection limit of the sensor is 0.9024 ppm.

The FTIR spectra of pure $SnO_2$ NBs and Y-$SnO_2$ NBs at room temperature are shown in Fig. 8. It is well known that FTIR is a powerful tool to identify functional groups or the types of chemical bonds. It is clearly seen that the peaks appear at around 561, 660, and 1628 $cm^{-1}$ for pure $SnO_2$. The spectrum of $SnO_2$ NBs contains resonance stretching vibration modes in the range of 400–800 $cm^{-1}$. The peaks at 561 and 660 $cm^{-1}$ belong to the Sn–O stretching vibration modes [25, 26]. A weak peak at 1628 $cm^{-1}$ is recognized as the deformation mode of OH groups [27]. We can also find that the increment of Y content causes a small shift to a lower wave number and the absorption peak becomes stronger. Some literatures have been reported to study the acetone absorption spectrum of gas sensor [28–30]. For example, Zhang et al. reported that the absorption peaks at 3582, 2968, 1731, 2929, and 1234 $cm^{-1}$ were detected [28–30] as $SnO_2$ sensor is exposed to acetone and then absorbs acetone vapor on its surface. Those vibration peaks could be assigned to the absorbed acetone $\nu$(OH), $\nu$(C–H), $\nu$(C=O), and $\nu$(C–C), respectively [28]. However, FTIR absorption peaks of Y-$SnO_2$ NBs located at 2930 and 3429 $cm^{-1}$ are close to the peak position of the absorbed acetone on the surface of the $SnO_2$ centered at 2929 and 3582 $cm^{-1}$, respectively. It shows that Y-$SnO_2$ sensor easily absorbs acetone. Therefore, the Y-$SnO_2$ NB sensor is sensitive to acetone, which supported the result of its sensing properties.

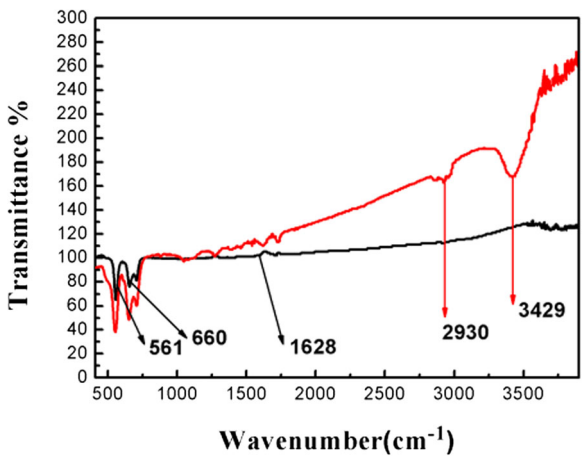


**Fig. 8** FTIR spectra of pure $SnO_2$ NBs and Y-$SnO_2$ NBs in the range of 400–4000 $cm^{-1}$

### Mechanism of the Sensitivity of Y-$SnO_2$ NBs

The sensitivity of oxide (n-type semiconductor oxide) nanobelt depends on the barrier height of its grain boundary, grain size, lattice defects, the amount of oxygen absorption on the surface, catalyst crystallinity, etc [31–33]. A lot of oxygen molecules are absorbed on the surface of $SnO_2$ NBs in air, resulting in the formation of a donor level and producing $O^-$ or $O^{2-}$ ions. The process is as follows:

$$O_2\ (gas) \rightarrow O_2\ (adsorption)$$
$$O_2\ (gas) \rightarrow O_2^-\ (adsorption)$$
$$O_2^-\ (gas) \rightarrow 2O^-\ (adsorption)$$
$$O_2^-\ (gas) \rightarrow O^{2-}\ (adsorption)$$

Nanometer sensor's surface is negatively charged and then leads to the free electron concentration of $SnO_2$ reduce so that the depletion layer is formed. The conductivity of metal oxide is dominated by the potential barrier formed at the grain boundaries. Reducing gas will react with the absorbed oxygen molecules when the gas sensor is exposed to the target gas so that released trapped electron will enter into the lattices of $SnO_2$. Thus, the barrier height decreases and its conductivity increases. For organic volatile acetone, the reaction process is expressed as follows:

$$4O_2^- + C_3H_6O = 3H_2O + 3CO_2 + 8e^-$$
$$8O^- + C_3H_6O = 3H_2O + 3CO_2 + 8e^-$$
$$8O^{2-} + C_3H_6O = 3H_2O + 3CO_2 + 16e^-$$

On the other hand, it is well known that doping can also lower the barriers' height and make the depletion layer thinner. These effects improve its electrical conductivity and enhance its sensing performances. The abovementioned mechanism can be depicted in Fig. 9.

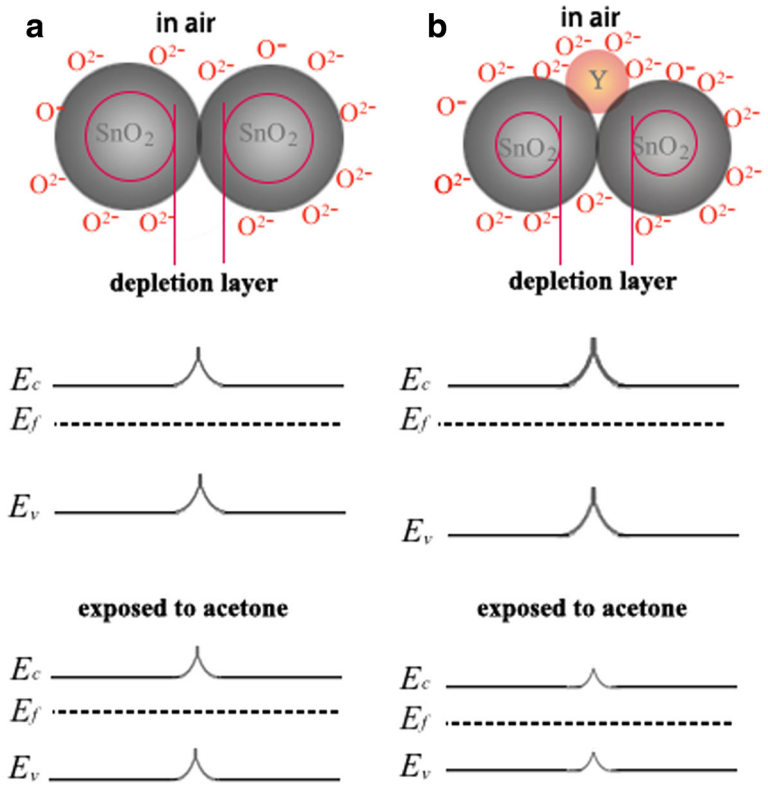


**Fig. 9** The sensing mechanism of Y-$SnO_2$ NBs in the acetone environment (**a**, **b**)

## Conclusions

Y-$SnO_2$ NBs have been synthesized by thermal evaporation method. The XRD pattern indicates that Y-$SnO_2$ NBs and undoped counterparts are a tetragonal structure. The EDS and XPS results reveal that $Y^{3+}$ ions are doped into $SnO_2$ NBs successfully. Compared with that of pure $SnO_2$, the UV-Vis absorption spectrum of Y-$SnO_2$ NBs redshifts after doping. In addition, the sensing property of the device based on Y-$SnO_2$ NB has been measured at different concentrations. It is found that the Y-$SnO_2$ NB device have a higher sensitivity with 11.4 to 100 ppm of acetone at 210 °C and the doping of Y improves the sensing performance of $SnO_2$ NBs effectively.

## Additional file

**Additional file 1:** Supporting information. (DOC 440 kb)

#### Acknowledgements

This work was supported by the National Natural Science Foundation of China (Grant No. 11164034), the Key Applied Basic Research Program of Science and Technology Commission Foundation of Yunnan Province (Grant No. 2013FA035), and the Innovative Talents of Science and Technology Plan Projects of Yunnan Province (Grant No. 2012HA007).

#### Authors' Contributions

YL guided the experiments and the test process and revised the paper. LX carried out the synthesis of nanobelts and gas sensitivity test and prepared the manuscript. LS, WY, and HJ carried out the characterization. YD analyzed the data. All authors read and approved the final manuscript.

#### Competing Interests

The authors declare that they have no competing interests.

#### Author details

[1]Key Laboratory of Yunnan Higher Education Institutes for Optoelectronic Information and Technology, Kunming 650500, People's Republic of China. [2]Key Laboratory of Yunnan Normal University for Photoelectric Materials & Device, Kunming 650500, People's Republic of China. [3]Institute of Physics and Electronic Information, Yunnan Normal University, Kunming 650500, People's Republic of China. [4]Department of Physics, State Key Laboratory for Mesoscopic Physics, Peking University, Beijing 100871, People's Republic of China.

Received: 27 September 2016 Accepted: 7 October 2016
Published online: 21 October 2016

#### References

1. Elisabetta C, Camilla B, Isabella C, Guido F, Matteo F, Matteo F et al (2013) Metal oxide nanoscience and nanotechnology for chemical sensors. Sens Actuators B 179:3–20
2. Wang Z, Luan D, Boey FY, Lou XW (2011) Fast formation of $SnO_2$ nanoboxes with enhanced lithium storage capability. J Am Chem Soc 133:4738–4741
3. Sambasivama S, Kim SB, Jeong JH, Choi BC, Lim KT, Kim SS, Song TK (2010) Effect of $Er^{3+}$ doping in $SnO_2$ semiconductor nanoparticles synthesized by solgel technique. Curr Appl Phys 10:1383–1386

4. Chen XB, Liu L, Yu PY, Mao SS (2011) Increasing solar absorption for photocatalysis with black hydrogenated titanium dioxide nanocrystals. Science 331:746–750
5. Ahn JH, Yun J, Choi YK, Park IK (2013) Palladium nanoparticle decorated silicon nanowire field-effect transistor with side-gates for hydrogen gas detection. Appl Phys Lett 104:013508
6. Fang TH, Chang WJ (2005) Nanomechanical characteristics of $SnO_2$: F thin films deposited by chemical vapor deposition. Appl Surf Sci 252: 1863–1869
7. Xu K, Zeng DW, Tian SQ, Zhang SP, Xie CS (2014) Hierarchical porous $SnO_2$ micro-rods topologically transferred from tin oxalate for fast response to trace formaldehyde. Sens Actuators B 190:585–592
8. Ma J, Liu YK, Zhang H, Ai P, Gong NL, Zhang Y (2014) Synthesis and high sensing properties of a single Pd-doped $SnO_2$ nanoribbon. Nanoscale Res Lett 9:503
9. Luo LB, Liang FX, Jie JS (2011) Sn-catalyzed synthesis of $SnO_2$ nanowires and their optoelectronic characteristics. Nanotechnology 22:485701
10. Ge LQ, Ji JY, Tian T, Xiao ZD, Gu ZZ, Norimatsu T, Shimada T, Nishimura H, Fujioka S, Nagai K (2010) Fabrication of the hollow $SnO_2$ nanoparticles contained spheres as extreme ultraviolet (EUV) target. Colloids Surf A 358:88–92
11. Ding JJ, Wang MQ, Yan XB, Zhang XY, Ran CX, Chen HX, Yao X (2013) Microstructures, surface states and field emission mechanism of graphene-tin/tin oxide hybrids. J Colloid Interf Sci 395:40–44
12. Hwang IS, Kim SJ, Choi JK, Jung JJ, Yoo DJ, Dong KY, Ju BK, Lee JH (2012) Large-scale fabrication of highly sensitive $SnO_2$ nanowire gas sensors by single step vapor phase growth. Sens Actuators B 165:97–103
13. Luo LB, Wang XH, Xie C, Li ZJ, Lu R, Yang XB, Lu J (2014) One-dimensional CuO nanowire: synthesis, electrical, and optoelectronic devices application. Nanoscale Res Lett 9:637
14. Manjula P, Arunkumar S, Manorama SV (2011) Au/$SnO_2$ an excellent material for room temperature carbon monoxide sensing. Sens Actuators B 152:168–175
15. Wang KW, Kang WD, Wei YC, Liu CW, Su PC, Chen HS, Chung SR (2011) Promotion of PdCu/C catalysts for ethanol oxidation in alkaline solution by $SnO_2$ modifier. Chemcatchem 4:1154–1161
16. Bhaumik S, Ray SK, Das AK (2013) Optical and magnetic properties of Er-doped $SnO_2$ nanoparticles. Appl Mater Sci 210:2146–2152
17. Lin YH, Chi YC, Lin GR (2013) Nanoscale charcoal powder induced saturable absorption and mode-locking of a low-gain erbium-doped fiber-ring laser. Laser Phys Lett 10:055105
18. Zhang X, Lin T, Zhang P, Xu J, Lin S, Xu L, Chen K (2014) Highly efficient near-infrared emission in $Er^{3+}$ doped silica films containing size-tunable $SnO_2$ nanocrystals. Opt Express 22:369–376
19. Song P, Wang Q, Yang ZX (2012) Preparation, characterization and acetone sensing properties of Ce-doped $SnO_2$ hollow spheres. Sens Actuators B 173: 839–846
20. Li SH, Liu YK, Wu YM, Chen WW, Qin ZJ, Gong NL, Yu DP (2016) Highly sensitive formaldehyde resistive sensor based on a single Er-doped $SnO_2$ nanobelt. Phys B 489:33–38
21. Huang H, Tian S, Xu J, Xie Z, Zeng D, Chen D, Shen G (2012) Needle-like Zn-doped $SnO_2$ nanorods with enhanced photocatalytic and gas sensing properties. Nanotechnology 23:105502
22. Fan F, Kanjanaboos P, Saravanapavanantham M, Beauregard E, Ingram G et al (2015) Colloidal $CdSe_{1-x}S_x$ nanoplatelets with narrow and continuously-tunable electroluminescence. Nano Lett 15:4611–4615
23. Ahmad MK, Mokhtar SM, Soon CF, Nafarizal N, Suriani AB, Mohamed A et al (2016) Raman investigation of rutile-phased $TiO_2$ nanorods/nanoflowers with various reaction times using one step hydrothermal method. J Mater Sci-Mater El 27:7920–7926
24. Liu H, Li M, Voznyy O, Hu L, Fu QY, Zhou DX, Xia Z et al (2014) Physically flexible, rapid-response gas sensor based on colloidal quantum dot solids. Adv Mater 26:2718–2724
25. Kuantama E, Han DW, Sung YM, Song JE, Han CH (2009) Structure and thermal properties of transparent conductive nanoporous F: $SnO_2$ films. Thin Solid Films 517:4211–4214
26. Zhang B, Tian Y, Zhang JX, Cai W (2010) The characterization of fluorine doped tin oxide films by fourier transformation infrared spectrum. Mater Lett 64:2707–2709
27. Sagadevan S, Podder J (2016) Investigation on structural, surface morphological and dielectric properties of Zn-doped $SnO_2$ nanoparticles. Mater Res 19:420–425
28. Zhang ZX, Huang KJ, Yuan FL (2014) Gas sensing properties and in situ diffuse reflectance infrared Fourier transform spectroscopy study of acetone adsorption and reactions on $SnO_2$ films. Sens Mater 26:649–663
29. Herrebout WA, Delanoye SN, Maes BUW, van der Veken BJ (2006) Infrared spectra of the complexes of trifluoroethene with dimethyl ether, acetone, and oxirane: a cryosolution study. J Phys Chem A 110:13759–13768
30. Wan LY, Li XY, Qu ZP, Shi Y, Li H, Zhao QD, Chen GH (2010) Facile synthesis of ZnO/$Zn_2TiO_4$ core/shell nanowires for photocatalytic oxidation of acetone. J Hazard Mater 184:864–868
31. Nie BA, Hu JG, Luo LB, Xie C, Zeng LH, Lv P, Li FZ, Jie JS, Feng M, Wu CY, Yu YQ, Yu SH (2013) Monolayer graphene film on ZnO nanorod array for high-performance schottky junction ultraviolet photodetectors. Small 9:2872–2879
32. Liu Y, Koep E, Liu ML (2005) Highly sensitive and fast-responding $SnO_2$ sensor fabricated by combustion chemical vapor deposition. Chem Mater 17:3997–4000
33. Maiti A, Rodriguez JA, Law M, Kung P, Mckinney JR, Yang PD (2003) $SnO_2$ nanoribbons as $NO_2$ sensors: insights from first principles calculations. Nano Lett 3:1025–1028